A Model of High-latitude Thermospheric Density

Yosuke Yamazaki[1], Michael J. Kosch[1,2], and Eric K. Sutton[3]

Physcs Dept., Lancaster University, Lancaster LA1 4YB, UK. (y.yamazaki@lancaster.ac.uk)

[1]Department of Physics, Lancaster University, Lancaster LA1 4YB, UK

[2]South African National Space Agency, Hermanus 7200, South Africa

[3]AFRL, Kirtland Air Force Base, New Mexico, USA

Abstract.

We present an empirical model of the high-latitude air density at 450 km, derived from accelerometer measurements by CHAMP and GRACE satellites during 2002-2006, which we call HANDY (*H*igh-latitude *A*tmospheric *N*eutral *D*ensit*Y*). HANDY consists of a quiet model and disturbance model. The quiet model represents the background thermospheric density for "zero geomagnetic activity" conditions. The disturbance model represents the response of the thermospheric density to solar wind forcing at high latitudes. The solar wind inputs used are the following: (1) solar wind electric field E_{SW}, (2) interplanetary magnetic field (IMF) clock angle C_{SW}, and (3) solar wind dynamic pressure P_{SW}. Both quiet and disturbance models are constructed on the basis of spherical harmonic function fitting to the data. Magnetic coordinates are used for the disturbance model, while geographical coordinates are used for the quiet model. HANDY reproduces main features of the solar wind influence on the high-latitude thermospheric density, such as the IMF B_y effect that produces a hemispheric asymmetry in the density distribution.

1. Introduction

The magnetosphere-ionopshere-thermosphere system is under significant influence of the solar wind at high latitudes. Deposition of the energy and momentum from the solar wind results in heating of the upper atmosphere, causing the thermosphere to expand. The density of the thermosphere increases at a fixed altitude as the thermal expansion brings molecular-rich air to higher levels. During geomagnetic storms, the thermospheric density can increase by several hundred percent in comparison with quiet periods [e.g., *Liu and Lühr*, 2005; *Sutton et al.*, 2005; *Bruinsma et al.*, 2006], which is an obvious concern for operators of low Earth orbit (LEO) satellites.

Various empirical models have been proposed to describe temperature and density variability in the thermosphere. The following are examples: Mass Spectrometer Incoherent Scatter Radar Extended (MSISE) models [*Hedin*, 1991; *Picone et al.*, 2002]; Drag Temperature Model (DTM) [*Bruinsma et al.* 2003; 2012]; Jacchia-Bowman (JB) models [*Bowman et al.*, 2008a, b]; and CHAMP empirical model [*Liu et al.*, 2013]. Those models evaluate the air density as a function of altitude, latitude, longitude, solar time, solar and geomagnetic activities, and day of year. The models are useful not only for satellite operations (i.e., orbital tracking and prediction) but also for characterizing the nature of thermospheric variability.

The previous models have been focused at low latitudes. Low latitudes account for substantial area of the globe, and thus it has been the primary interest for scientists and satellite operators. Besides, in-situ satellite measurements have been sparse at high latitudes, as it requires the satellite to be in a high-inclination orbit. Consequently, the three

dimensional models mentioned above do not include high-latitude density features. This issue was brought to light when *Liu et al.* [2005] compared thermospheric densities measured by the CHAllenging Minisatellite Payload (CHAMP) satellite [*Reigber et al.*, 2002] with the MSISE-90 model [*Hedin*, 1991]. *Liu et al.* [2005] showed that the MSISE-90 model fails to reproduce high-latitude density structures observed by the CHAMP satellite. The discrepancy was especially evident at magnetic high latitudes around the noon sector and pre-midnight sector where the MSISE-90 model significantly underestimates the air density. The MSISE-90 model, like other global models of the thermosphere, is based on fitting of low-order global spherical functions to observations, which tend to smooth out relatively small structures at high latitudes.

Air drag measurements by CHAMP have revealed high-latitude thermospheric density distributions in great detail. The high-inclination near-circular orbit of CHAMP (I=87°) enabled pole-to-pole measurements during its operation from July, 2000 through September, 2010. *Lühr et al.* [2004] found a region of enhanced thermospheric density at high latitudes, around the dayside cusp. It was later realized that the amplitude of this density bulge is largely controlled by the magnitude of the solar wind electric field [e.g., *Rentz and Lühr*, 2008; *Kervalishvili and Lühr*, 2014] and the orientation of the interplanetary magnetic field (IMF) [*Kwak et al.*, 2009; *Yamazaki et al.*, 2015]. Numerical studies have shown that the cusp-region density enhancement could arise from local heating due to soft electron precipitation and Poynting flux [*Crowley et al.*, 2010; *Li et al.*, 2011; *Zhang et al.*, 2012; *Deng et al.*, 2013].

Extensive high-latitude measurements by CHAMP also revealed a region of relatively enhanced thermospheric density in the night-time sector around 22-01 magnetic local

time, which is associated with substorms [*Ritter et al.*, 2010]. The simulation study by *Zhang et al.* [2012] showed that soft electron precipitation increases the thermospheric density not only in the dayside cusp region, but also in the pre-midnight region.

The Gravity Recovery and Climate Experiment (GRACE) satellite [*Tapley et al.*, 2004] has also collected a large quantity of thermospheric density data in a high-inclination (I=89°) near-circular orbit since March, 2002. The GRACE altitude was higher than CHAMP's by some 100 km during the period when both GRACE and CHAMP were operative. *Lei et al.* [2012] explored density data from the two satellites, normalizing those data into a single fixed height at 400 km. This way, they were able to improve the horizontal spatial coverage of the data, which facilitates the separation between spatial and temporal variability. In the present study, we also use thermospheric density data from CHAMP and GRACE. The main focus of this paper is to present the first model of the high-latitude thermospheric density at 450 km that uses solar wind parameters as inputs. The model results are discussed in comparison with previous results in the literature.

2. Data and Model Construction

We analyze thermospheric total mass densities, derived from the CHAMP and GRACE accelerometer data. The density retrieval procedures and error evaluations were detailed in *Sutton* [2008]. Briefly, the overall accuracy of the data is ∼11%. Errors mainly come from the drag coefficient, neglect of winds, and instrument calibration. The error from neglecting winds is typically 2-10%, but at high latitudes during storms, the error can be up to ∼25%. The error due to the precision of the accelerometer is less than 1%.

We use the data for four years from August, 2002 through July, 2006, when both satellites were operating. During this period the CHAMP satellite gradually descended from approximately 420 km to 350 km, and the GRACE altitude was around 500-480 km, as shown in Figure 1 (top). All the data from the two satellites at different altitudes were normalized at a single height of 450 km, which is approximately in the middle of the two satellites. The MSISE-00 model was used for the altitude corrections. As discussed in previous studies [*Forbes et al.*, 2009, 2011; *Lei et al.*, 2012], it is necessary to inter-calibrate CHAMP and GRACE densities before the two data sets are combined. Following these studies, we first computed the mean ratio between CHAMP measurements and MSISE-00 model, as well as the mean ratio between GRACE measurements and MSISE-00 model. A correction factor was, then, determined so as to adjust one of the obtained ratios to the other. An analysis indicated the following relationship: $\overline{\text{GRACE/MSISE}}$=0.897*$\overline{\text{CHAMP/MSISE}}$.

The period of our data analysis was limited to four years (August, 2002 to July, 2006). This choice was made as a compromise between including as much data as possible and eliminating measurements in which the CHAMP altitude was too low compared to the target height of 450 km. Besides, studies showed that the MSISE-00 model was not accurate during the extreme solar minimum of 2008–2009 owing to an unexpectedly large amount of helium [*Thayer et al.*, 2012; *Liu et al.*, 2014a], which would affect our height corrections based on MSISE-00.

The period we investigate (i.e., 2002–2006) is in the declining phase of solar cycle 23. Figure 1 (middle) shows monthly mean values of the $M_{10.7}$ index, which is the Mg II core-to-wing ratio [*Viereck et al.*, 2001] scaled to the $F_{10.7}$ index. We derived $M_{10.7}$ based on a

linear least squares fit of daily $F_{10.7}$ to the corresponding Mg II values, following *Solomon et al.* [2011]. Daily values of the $M_{10.7}$ index will be used later as an input parameter of our models. Monthly mean *ap* index is plotted in Figure 1 (bottom), representing geomagnetic activity during 2002–2006. As is known, the declining phase of a solar cycle provides relatively high geomagnetic activity [e.g., *Lockwood et al.*, 1999], which is favorable for the purpose of our investigation.

Our model, HANDY (*H*igh-latitude *A*tmospheric *N*eutral *D*ensit*Y*), was constructed in terms of the logarithm of the air density (not the absolute density), as is the case for most empirical models of the thermosphere. The analysis in terms of log-density (or relative density changes) is more appropriate for empirical modeling than the analysis in terms of absolute density. This is primarily owing to the fact that variance of absolute density varies significantly through a solar cycle. The variance of absolute density increases with increasing solar activity as the background density undergoes an order-of-magnitude increase from solar minimum to solar maximum. Since ordinary least-squares fitting assumes uniform variance, if absolute density were chosen to use for the fitting, the solar maximum data would receive much greater weight in the fit than the solar minimum data. This problem can be avoided by using log density, as its variance is much more uniform through a solar cycle. Further discussion on the advantage of log-density over absolute density in climatological studies can be found in the paper by *Emmert and Picone* [2010, section 2.2].

The construction of the model involves two steps. First, we created a global quiet model, which represents the background density for "zero geomagnetic activity" conditions. The quiet model was, then, subtracted from the original data. The residuals were analyzed

focusing on high latitudes in order to construct a disturbance model, which represents the response of the high-latitude thermosphere density to solar wind forcing. Letting ρ_M represent the model density,

$$\log \rho_M = \log \rho_q + \log \rho_d \quad (1)$$

where $\log \rho_q$ is the quiet model and $\log \rho_d$ is the disturbance model. It is obvious, from Eq (1), the construction of the disturbance model is, in effect, to model the relative density perturbation from the quiet-time background density, i.e., $\rho_d \sim \rho/\rho_q$.

We use geographical coordinates for the quiet model and magnetic coordinates for the disturbance model. The quiet-time background density is primarily controlled by solar heating, and thus geographical coordinates are suitable to describe the density distribution and variability. On the other hand, density perturbations during geomagnetically disturbed periods arise mainly from high-latitude Joule heating and other processes of magnetosphere-ionosphere-thermosphere coupling, which are better organized in magnetic coordinates than in geographical coordinates. Specifically, we use magnetic apex coordinates described by *Richmond* [1995] and *Emmert et al.* [2010].

2.1. Quiet Model

The quiet model was constructed in the following way. First, we collected all the CHAMP and GRACE data when the average of the *ap* index during the last 24 h is less than 9 nT (equivalently $Kp \leq 2$). Next, these quiet-day measurements were evaluated as a function of geographic latitude, longitude, universal time, local time, day of year, solar activity, and geomagnetic activity. The equations used for the quiet model are basically the same as the MSISE-00 model, which were detailed in *Hedin* [1983, 1987]. The differences are that we use the $M_{10.7}$ index instead of the $F_{10.7}$ index and that the

dependence of log-densities on the daily *ap* index is simplified considering only the linear dependence. (The exact formula for the quiet model is shown in the auxiliary material.) Previous studies found that the $M_{10.7}$ index is able to represent the solar activity influence on the thermosphere, often better than $F_{10.7}$ [e.g., *Guo et al.*, 2007]. The dependence of the density on geomagnetic activity is fairly small for *ap* <9 nT, which can be assumed to be linear [e.g., *Vickers et al.*, 2013].

Fitting coefficients were determined using the least squares technique. The quiet model of HANDY is then obtained by normalizing the reconstructed densities to *ap* =0 nT, which gives density estimates for the zero geomagnetic activity condition. It is noted that the zero geomagnetic activity condition defined above does not mean that the energy input from the solar wind to the upper atmosphere is actually zero. Generally, the high-latitude atmosphere is subject to solar wind disturbances even when *ap* =0 nT. The zero geomagnetic activity condition merely gives an objective reference level of geomagnetic activity for the density perturbation.

As is clear from the analysis procedure, our quiet model is designed to be consistent with the MSISE-00 model at *ap* =0 nT. We demonstrate in Figure 2 that seasonal and solar-activity variations in the density are in good agreement between our quiet model and the MSISE-00 model (at *ap* =0 nT). The plots are limited to poleward of ±60° latitude, as we are interested in high latitudes only. Both models show a strong dependence on solar activity. The enhanced solar EUV heating during solar maximum increases the thermospheric temperature, which leads to an increase of the density at a fixed altitude. The density tends to be greater in the summer hemisphere than in the winter hemisphere, which is due to higher solar insolation in summer. High-latitude densities are comparable

between the Northern and Southern Hemispheres under the equinoctial condition. The effect of solar insolation also explains the daily variation of the density, causing greater densities during daytime than nighttime.

The top panels in Figure 3 compare the quiet model with the original measurements at high magnetic latitudes (poleward of $\pm 60^\circ$ magnetic latitude). As expected, the quiet model accounts a substantial part of the density but slightly underestimates the measurements as it does not include contributions of geomagnetic activity. A study by *Emmert and Picone* [2010] showed that more than 90% of global density perturbations can be attributed to the effect of solar activity and solar insolation (i.e., solar time and season).

It is known that the composition of the high-latitude thermosphere varies significantly with solar activity and season. According to MSISE-00, the neutral population at 450 km is dominated by atomic oxygen (O), which accounts for $\sim$90% of the total mass on average. The other 10% is mainly by helium (He) and molecular nitrogen (N_2). The contribution of He can be over 50% in the winter hemisphere under low solar and geomagnetic activity conditions owing to the existence of the winter helium bulge [See *Liu et al.*, 2014b and references therein]. Different constituents have different response to geomagnetic activity. Thus, although we do not have composition data for the present study, the change in the composition is expected to add complexity to the thermospheric response to solar wind forcing described in the following section. (See also *Thayer et al.* [2012] for the composition effect on the total mass density at CHAMP and GRACE altitudes.)

2.2. Disturbance Model

We analyzed the residuals between the measurements and quiet model estimates for the disturbance model. The model was constructed separately for the Northern Hemisphere

and Southern Hemisphere in the apex magnetic coordinates. Our approach is somewhat similar to that of *Weimer* [1995, 1996], who constructed empirical models of the high-latitude potential electric field on the basis of a spherical cap harmonic analysis. Following *Weimer* [1995, 1996], the lower boundaries were set to ±45° magnetic apex latitudes, and spherical harmonic functions were fitted to the data only poleward of the boundaries. The model formulation is as follows:

$$\log \rho_d \left(MLAT, MLT\right) = \sum_{l=0}^{6} \sum_{m=0}^{min(l,3)} \left(A_{lm} \cos \frac{2\pi m}{24} MLT + B_{lm} \sin \frac{2\pi m}{24} MLT \right) P_{lm} \left(\nu\right) \tag{2}$$

where $MLAT$ is apex magnetic latitude in degrees, and MLT is magnetic local time in hours. A_{lm} and B_{lm} are functions of solar wind parameters, which will be discussed later. P_{lm} is the Schmidt normalized associated Legendre function with order l and degree m, expressed as follows:

$$P_{lm}(\nu) = s(1-\nu^2)^{\frac{m}{2}} \frac{\partial^m}{\partial \nu^m} \left[\frac{1}{l! 2^l} \frac{d^l}{d\nu^l} \left(\nu^2 - 1\right) \right] \tag{3}$$

where s=1 for $m = 0$, and $s = \left[2\frac{(l-m)!}{(l+m)!}\right]^{\frac{1}{2}}$ for m>0, and ν is a function of $MLAT$, given as:

$$\nu = \cos \left[(90 - MLAT) \frac{\pi}{45} \right] \tag{4}$$

Thus, ν varies from 1 at the North Pole to -1 at the lower boundary of 45° in the Northern Hemisphere, and from 1 at the South Pole to -1 at the lower boundary of at -45° in the Southern Hemisphere. The spherical harmonic expansion was truncated at l=6 and m=3. The inclusion of higher order/degree terms does not add any new steady structure but tends to exaggerate noise. It is noted that the quiet model also uses spherical harmonics truncated at l=6 and m=3. An important difference between the quiet model and dis-

turbance model is that the quiet model is based on a global fitting while the disturbance model is based on a regional fitting (i.e., poleward of ±45° magnetic apex latitudes). By limiting the area of fitting, we ensure that the disturbance model can properly capture density structures in the high-latitude regions.

The A_{lm} and B_{lm} terms in Equation (2) are functions of the following: solar wind electric field magnitude E_{SW}, solar wind dynamic pressure P_{SW}, IMF clock angle C_{SW}, solar activity M, and day of year DoY. For the solar activity parameter M, we use the daily value of the $M_{10.7}$ index one day prior to the observed density. For the solar wind parameters, we used 1-min OMNI solar wind data adjusted to the Earth's bow shock nose. An additional time delay of 15 min was added to account for the magnetosphere-ionosphere distance [*Vennerstrøm et al.*, 2002; *Rentz and Lühr*, 2008]. We tested various combinations of averaging window widths and time lags using the CHAMP and GRACE data for the polar regions above ±60° magnetic latitude. The best fit was obtained when the solar wind data are averaged for the past 10 hours from the present time. Any time lag from the 15-min adjustment did not improve the fitting. The suitable time lag may be different at other latitudes, as the time lag for the thermospheric density response to solar wind disturbances is generally larger at lower latitudes [*Sutton et al.*, 2009].

235 Mathematical expressions for A_{lm} and B_{lm} were determined on a trial and error basis.

236 So far, the best model performance was obtained using the following:

$$
\begin{aligned}
C_{lm} = {} & \alpha_1^{lm} + \alpha_2^{lm}\sqrt{E_{SW}} + \alpha_3^{lm}\sqrt{P_{SW}} + \alpha_4^{lm} M \\
& + \sum_{k=1}^{2}\left[\beta_{2k-1}^{lm}\cos\left(kC_{SW}\right) + \beta_{2k}^{lm}\sin\left(kC_{SW}\right)\right] + \sum_{k=1}^{2}\left[\gamma_{2k-1}^{lm}\cos\left(kDoY\right) + \gamma_{2k}^{lm}\sin\left(kDoY\right)\right] \\
& + \sqrt{E_{SW}}\left(\sigma_1^{lm} M + \sum_{k=1}^{2}\left[\epsilon_{2k-1}^{lm}\cos\left(kC_{SW}\right) + \epsilon_{2k}^{lm}\sin\left(kC_{SW}\right)\right]\right. \\
& \qquad \left. + \sum_{k=1}^{2}\left[\zeta_{2k-1}^{lm}\cos\left(kDoY\right) + \zeta_{2k}^{lm}\sin\left(kDoY\right)\right]\right) \\
& + \sqrt{P_{SW}}\left(\eta_1^{lm} M + \sum_{k=1}^{2}\left[\theta_{2k-1}^{lm}\cos\left(kC_{SW}\right) + \theta_{2k}^{lm}\sin\left(kC_{SW}\right)\right]\right. \\
& \qquad \left. + \sum_{k=1}^{2}\left[\iota_{2k-1}^{lm}\cos\left(kDoY\right) + \iota_{2k}^{lm}\sin\left(kDoY\right)\right]\right)
\end{aligned}
\tag{5}
$$

238 where C_{lm} is either A_{lm} or B_{lm}. We found that the use of $\sqrt{E_{SW}}$ and $\sqrt{P_{SW}}$ improves the
239 fitting, compared to the results with E_{SW} and P_{SW}. As will be shown later, $\log \rho_d$ does
240 not linearly increase with E_{SW} and P_{SW}.

241 The coefficients α^{lm}, β^{lm}, γ^{lm}, δ^{lm}, ϵ^{lm}, ζ^{lm}, η^{lm}, θ^{lm}, and ι^{lm} were determined for A_{lm}
242 and B_{lm}, separately in the Northern Hemisphere and the Southern Hemisphere, using the
243 least squares method. The model coefficients are included in the auxiliary material, with
244 corresponding 1σ errors evaluated using the bootstrap method.

3. Model Results and Discussion

3.1. Comparison with Other Models

245 The middle panels in Figure 3 show good agreement between the final model estimates
246 (i.e., the quiet model plus disturbance model) and CHAMP/GRACE measurements at
247 high magnetic latitudes. The goodness of fit, evaluated as the square of the correlation
248 coefficient, is 0.90 in the Northern Hemisphere and 0.91 in the Southern Hemisphere. The

root-mean-square error, defined here as $\sqrt{(\log\rho - \log\rho_M)^2}$, is plotted in the bottom panels in Figure 3. The results indicate that the average root-mean-square error for the HANDY model is 15.0% in the Northern Hemisphere and 15.6% in the Southern Hemisphere during the period investigated. As can be seen in Figure 3 (bottom), the performance of HANDY does not significantly depend on solar activity or season. On the other hand, the root-mean-square error for the MSISE-00 model shows seasonal variations, indicating poor performance during local summer. The average error for MSISE-00 is 21.5% and 24.1% in the Northern Hemisphere and Southern Hemisphere, respectively. The larger error for MSISE-00 than HANDY is partly due to the fact that MSISE-00 does not include CHAMP/GRACE data in fitting while HANDY does. Thus, we also calculated the root-mean-square errors for the JB2008 model [*Bowman et al.*, 2008b], which is constrained by CHAMP and GRACE data (2001–2005). The results are shown in Figure 3 (bottom). The average error for JB2008 is 19.0% in the Northern Hemisphere and 19.4% in the Southern Hemisphere. Previous studies have reported that the JB2008 model generally performs slightly better than the MSISE-00 model [*Bowman et al.*, 2008b; *Shim et al.*, 2012].

Figure 4 shows the high-latitude density response to geomagnetic/solar-wind disturbances in the Northern Hemisphere (top) and in the Southern Hemisphere (bottom) for the September equinox condition. The left panels are for the MSISE-00 model, and the right panels are for the HANDY model. For the MSISE-00 results, the color indicates the density ratio between ap=27 nT (equivalently Kp=4) and ap=0 nT for a moderate solar activity condition ($F_{10.7}$=135 sfu). The HANDY results are produced for the following solar wind inputs: E_{SW}=3.3 mV/m, P_{SW}=3.1 hPa, and C_{SW}=180°. These E_{SW} and

P_{SW} values correspond to geomagnetic activity of ap=27 nT on average. It is immediately obvious in Figure 4 that there are significant discrepancies between the MSISE-00 and HANDY results. The HANDY results indicate regions of locally enhanced and reduced response around the noon sector and pre-dawn sector, respectively, which are completely missing from the MISISE-00 results. The weak response around the pre-dawn sector is interesting, as it is indeed where Joule heating from the closure of magnetic field-aligned currents peaks [*Weimer*, 2005]. *Yamazaki et al.* [2015] discussed that the production rate of nitric oxide, which is a strong radiative coolant, may be locally enhanced due to precipitation of hard electrons. This mechanism needs to be validated by independent measurements.

Another clear discrepancy is that HANDY predicts the largest increase in the relative density in the pre-midnight sector, while the MSISIE-00 shows it after the midnight. It should be noted that the MSIS-00 model uses geographical coordinates while the disturbance model of HANDY uses magnetic coordinates. However, the difference in the coordinates does not seem to explain all the differences between the MSISE-00 and HANDY results. The pre-midnight sector is where substorm onset is often observed [e.g., *Frey et al.*, 2004]. Heating due to energetic particle precipitation during substorms may be a reason for the density enhancement in this region. The solar wind response in HANDY is in general agreement with other climatological studies [e.g., *Liu et al.*, 2005; *Rentz and Lühr*, 2008; *Kervalishvili and Lühr*, 2013].

3.2. Dependence on Solar Wind Drivers

In order to provide insight into how the relative density ρ_d varies with the solar wind electric field magnitude and solar wind dynamic pressure, we have run the HANDY model

for various E_{SW} and P_{SW} conditions. The calculations started with E_{SW}=1.7 mV/m, P_{SW}=1.9 hPa, C_{SW}=180°, $M_{10.7}$=120 sfu and DoY=264. These E_{SW} and P_{SW} values roughly correspond to ap=4 nT (or Kp=1). Then, in one of the runs, the E_{SW} value was increased up to 15.1 mV/s without changing the other parameters. In the other run, the P_{SW} value was increased up to 10.5 hPa while keeping the other parameters the same. These upper values for E_{SW} and P_{SW} correspond to approximately ap=208 nT (or Kp=8), i.e., a severe storm condition. The results are shown in Figure 5, where the relative density is averaged for poleward of ±60° magnetic latitude. As expected, the relative density increases with increasing E_{SW} in both the Northern and Southern Hemispheres. Since the equinox condition was assumed, the E_{SW} response is comparable in the two hemispheres. Later, we will show how the relative density changes with the IMF clock angle, solar activity and season. It can be seen in Figure 5 that the relative density approximately linearly changes with E_{SW}. This is why a non-linear function $\sqrt{E_{SW}}$ fitted better than E_{SW} to the log densities: See our model parameterization in Eq (5). The solar wind electric field is directly related to high-latitude ionospheric electric fields [e.g., *Shepherd*, 2002] and thus is a good indicator of the amount of the energy deposited from the solar wind to the magnetosphere-ionosphere-thermosphere system. The mechanisms by which the thermosphere density responses to the solar wind energy input were discussed in detail by *Lei et al.* [2010].

It is obvious from the results in Figure 5 that the HANDY attribution of density perturbations to P_{SW} is much smaller than that to E_{SW}. This indicates that the solar wind density makes a relatively small contribution to thermospheric density variability. It is noted that high-speed solar wind increases both E_{SW} and P_{SW}.

The dependence of the relative density on the IMF clock angle is depicted in Figure 6 for the Northern Hemisphere. The density response to the solar wind becomes greater as the IMF B_z changes from positive to negative. The overall pattern of the relative density remains the same for different C_{SW} conditions. Figure 7 shows the results for the Southern Hemisphere. Again, the IMF B_z control of the relative density is evident.

The IMF B_y also modulates the high-latitude density response to the solar wind. As we reported in the previous paper [*Yamazaki et al.*, 2015], the influence of the positive IMF B_y in the Northern Hemisphere resembles the influence of the negative IMF B_y in the Southern Hemisphere. In Figures 6 and 7, this effect is most evident in the density response in the dawn sector. In the Northern Hemisphere, the negative IMF B_y reduces the density response at dawn, while in the Southern Hemisphere the positive IMF B_y reduces the density response at dawn. Figure 8 illustrates, more clearly, the hemispheric asymmetry of the high-latitude thermospheric density due to IMF B_y. The density ratios for the negative to positive IMF B_y results show approximately the opposite pattern between the Northern Hemisphere and the Southern Hemisphere. It is noted that the results in Figure 8 vary little with solar activity and season. It is interesting to note that the pattern of the IMF B_y effect on the high-latitude thermosphere bears some resemblance with the average high-latitude electric potential pattern [e.g., *Weimer et al.*, 2005; *Cousins and Shepherd*, 2010]. That is, the regions of the large IMF B_y effect in Figure 8 roughly correspond to the regions of the maximum and minimum electric potential. The mechanism by which the IMF B_y affects the high-latitude density is not known, and hence further investigation will be necessary. One possible way is through the action of vertical winds. It is known that at high latitudes, the pattern of horizontal

winds depends on the IMF B_y [*Förster et al.*, 2008]. Changes in the horizontal wind system possibly alter vertical winds, which would affect the density by causing adiabatic heating or cooling and by altering the composition.

3.3. Dependence on the Background Density

Figure 9 shows the high-latitude thermospheric density response to the solar wind under different solar EUV activity conditions. It can be seen that relative density perturbations are slightly smaller when solar activity is higher. As we showed in Figure 2, the background thermospheric density changes by an order of magnitude due to changes in solar activity. The fact that the dependence of the relative density on solar activity is small indicates that solar activity affects not only the background density, but also the magnitude of density perturbations by a similar (but slightly smaller) rate. *Emmert and Picone* [2010] obtained similar results based on the analysis of the global average thermospheric density. They discussed that the reduced density response during high solar activity period may result from mitigated temperature perturbations due to increased scale height.

The seasonal variation in the relative density is illustrated in Figure 10. The relative density tends to be small during local summer when the background density is relatively high. Previous studies have shown that the response of the absolute density to geomagnetic activity tends to be comparable in the Northern Hemisphere and the Southern Hemisphere [e.g., *Liu and Lühr*, 2005; *Yamazaki et al.*, 2015].

3.4. Summary and Conclusions

Using extensive accelerometer data by the CHAMP and GRACE satellites, we have constructed the first model to reproduce the response of the high-latitude thermospheric

density to solar wind forcing. We call the model HANDY. HANDY is composed of a quiet model and disturbance model. Both are created at an altitude of 450 km. The quiet model represents the background density, and it was designed to be consistent with the MSISE-00 for the zero geomagnetic activity (ap=0 nT) condition. The disturbance model represents relative density variations, from the quiet-time background, due to forcing by the solar wind. HANDY has new features that other global thermosphere models do not have, such as the use of solar wind parameter inputs (in contrast to conventional geomagnetic activity inputs) and the use of magnetic apex coordinates along with geographical coordinates.

The root mean square error for the HANDY model is approximately 15% during the period of investigation. A comparison with other commonly used models indicates that the HANDY performance is reasonably good. (The corresponding error is ∼23% for the MSISE-00 model and ∼19% for the JB2008 model.) It should be noted, however, that the data we analyzed for the HANDY construction was limited for August, 2002 – July, 2006, and thus the model is not constrained by the measurements around solar maximum or solar minimum. The representation of the solar cycle variation in the background density may be improved by including more data especially during high or low solar activity.

The HANDY results for the high-latitude density response to solar wind forcing are consistent with previous studies. The magnitude of relative density perturbations depends strongly on the solar wind electric field intensity and the orientation of the IMF. The response of the relative density to the solar wind electric field is most significant in the pre-midnight sector, where substorm onset often takes place. The solar wind response is relatively strong in the noon sector and relatively weak in the pre-dawn sector. These features are completely missing from the MSISE-00 model. Also, the HANDY results

clearly demonstrated the IMF B_y effect, which we found in the previous study [*Yamazaki et al.*, 2015]. The effect of the IMF B_y in the Northern Hemisphere is similar to that in the Southern Hemisphere for the opposite sense of the IMF B_y.

Although HANDY has been shown to be useful in revealing features of the high-latitude thermospheric density, the model restriction to a single altitude is an obvious disadvantage for practical purposes. One possible approach for the vertical extension of the model is to construct similar models at different altitudes and interpolate them, which would require a more extensive data set from various satellites at different heights. Another approach is to introduce an assumption on the height profile of the air density. Most global empirical models assumes diffusive equilibrium, which is a good approximation above ∼200 km. However, this approach requires knowledge of temperature and composition for at least two heights. We will leave the extension of HANDY for a topic of a future study.

Finally, the auxiliary material contains a document describing the model formats, along with lists of quiet and disturbance model coefficients with corresponding 1σ errors.

Acknowledgments.

The geomagnetic activity index *ap* was provided by the German Research Center for Geosciences, GFZ (http://www.gfz-potsdam.de/en/home). The Mg II core-to-wing ratio was provided by the Institute of Environmental Physics, University of Bremen (http://www.iup.uni-bremen.de/gome/gomemgii.html). The $F_{10.7}$ index was provided by the Herzberg Institute of Astrophysics. The hourly solar wind data were obtained from the NASA OMNIweb database (http://omniweb.gsfc.nasa.gov/). This work was supported by NERC grant NE/K01207X/1.

References

405 Bowman, B. R., W. K. Tobiska, F. A. Marcos, and C. Valladares (2008a), The JB2006
406 empirical thermospheric density model, *J. Atmos. Sol. Terr. Phys.*, *70*, 774–793,
407 doi:10.1016/j.jastp.2007.10.002.

408 Bowman, B. R., W. K. Tobiska, F. A. Marcos, C. Y. Huang, C. S. Lin, and W. J. Burke
409 (2008b), A new empirical thermospheric density model JB2008 using new solar and
410 geomagnetic indices, paper AIAA 2008–6438 presented at AIAA/AAS Astrodynamics
411 Specialist Conference and Exhibit, Am. Inst. of Aeronaut. and Astronaut., Honolulu.

412 Bruinsma, S., and G. Thuillier (2003), The DTM-2000 empirical thermosphere model with
413 new data assimilation and constraints at lower boundary: Accuracy and properties, *J.*
414 *Atmos. Sol. Terr. Phys.*, *65*, 1053–1070.

415 Bruinsma, S., J. M. Forbes, R. S. Nerem, and X. Zhang (2006), Thermosphere
416 density response to the 20–21 November 2003 solar and geomagnetic storm
417 from CHAMP and GRACE accelerometer data, *J. Geophys. Res.*, *111*, A06303,
418 doi:10.1029/2005JA011284.

419 Bruinsma, S. L., N. Sánchez-Ortiz, E. Olmedo, and N. Guijarro (2012), Evaluation of the
420 DTM-2009 thermosphere model for benchmarking purposes, *Journal of Space Weather*
421 *and Space Climate*, *2*(26), A04, doi:10.1051/swsc/2012005.

422 Cousins, E. D. P., and S. G. Shepherd (2010), A dynamical model of high-latitude con-
423 vection derived from SuperDARN plasma drift measurements, *J. Geophys. Res.*, *115*,
424 A12329, doi:10.1029/2010JA016017.

425 Crowley, G., D. J. Knipp, K. A. Drake, J. Lei, E. Sutton, and H. Lühr (2010), Thermo-
426 spheric density enhancements in the dayside cusp region during strong BY conditions,

427 *Geophys. Res. Lett.*, *37*, L07110, doi:10.1029/ 2009GL042143.

428 Deng, Y., T. J. Fuller-Rowell, A. J. Ridley, D. Knipp, and R. E. Lopez (2013), Theoretical
429 study: Influence of different energy sources on the cusp neutral density enhancement,
430 *J. Geophys. Res. Space Physics*, *118*, 2340–2349, doi:10.1002/jgra.50197.

431 Emmert, J. T., and J. M. Picone (2010), Climatology of globally averaged thermospheric
432 mass density, *J. Geophys. Res.*, *115*, A09326, doi:10.1029/2010JA015298.

433 Emmert, J. T., A. D. Richmond, and D. P. Drob (2010), A computationally compact rep-
434 resentation of Magnetic-Apex and Quasi-Dipole coordinates with smooth base vectors,
435 *J. Geophys. Res.*, *115*, A08322, doi:10.1029/2010JA015326.

436 Forbes, J. M., S. L. Bruinsma, X. Zhang, and J. Oberheide (2009), Surface-exosphere cou-
437 pling due to thermal tides, *Geophys. Res. Lett.*, *36*, L15812, doi:10.1029/2009GL038748.

438 Forbes, J. M., X. Zhang, S. Bruinsma, and J. Oberheide (2011), Sun-synchronous ther-
439 mal tides in exosphere temperature from CHAMP and GRACE accelerometer measure-
440 ments, *J. Geophys. Res.*, *116*, A11309, doi:10.1029/2011JA016855.

441 Förster, M., S. Rentz, W. Köhler, H. Liu, and S. E. Haaland (2008), IMF dependence of
442 high-latitude thermospheric wind pattern derived from CHAMP cross-track measure-
443 ments, *Ann. Geophys.*, *26*, 1581–1595.

444 Frey, H. U., S. B. Mende, V. Angelopoulos, and E. F. Donovan (2004), Substorm onset ob-
445 servations by IMAGE-FUV, *J. Geophys. Res.*, *109*, A10304, doi:10.1029/2004JA010607.

446 Guo, J., W. Wan, J. M. Forbes, E. Sutton, R. S. Nerem, T. N. Woods, S. Bruinsma,
447 and L. Liu (2007), Effects of solar variability on thermosphere density from CHAMP
448 accelerometer data, *J. Geophys. Res.*, *112*, A10308, doi:10.1029/2007JA012409.

Hedin, A. E. (1983), A Revised thermospheric model based on mass spectrometer and incoherent scatter data: MSIS-83, *J. Geophys. Res.*, *88*(A12), 10170–10188, doi:10.1029/JA088iA12p10170.

Hedin, A. E. (1987), MSIS-86 Thermospheric Model, *J. Geophys. Res.*, *92*(A5), 4649–4662, doi:10.1029/JA092iA05p04649.

Hedin, A. E. (1991), Extension of the MSIS Thermosphere Model into the middle and lower atmosphere, *J. Geophys. Res.*, *96*(A2), 1159–1172, doi:10.1029/90JA02125.

Kervalishvili, G. N. and Lühr, H. (2013), The relationship of thermospheric density anomaly with electron temperature, small-scale FAC, and ion up-flow in the cusp region, as observed by CHAMP and DMSP satellites, *Ann. Geophys.*, *31*, 541–554, doi:10.5194/angeo-31-541-2013.

Kwak, Y.-S., A. D. Richmond, Y. Deng, J. M. Forbes, and K.-H. Kim (2009), Dependence of the high-latitude thermospheric densities on the interplanetary magnetic field, *J. Geophys. Res.*, *114*, A05304, doi:10.1029/2008JA013882.

Lei, J., J. P. Thayer, A. G. Burns, G. Lu, and Y. Deng (2010), Wind and temperature effects on thermosphere mass density response to the November 2004 geomagnetic storm, *J. Geophys. Res.*, *115*, A05303, doi:10.1029/2009JA014754.

Lei, J., T. Matsuo, X. Dou, E. Sutton, and X. Luan (2012), Annual and semiannual variations of thermospheric density: EOF analysis of CHAMP and GRACE data, *J. Geophys. Res.*, *117*, A01310, doi:10.1029/2011JA017324.

Li, W., D. Knipp, J. Lei, and J. Raeder (2011), The relation between dayside local Poynting flux enhancement and cusp reconnection, *J. Geophys. Res.*, *116*, A08301, doi:10.1029/2011JA016566.

Liu, H., and H. Lühr (2005), Strong disturbance of the upper thermospheric density due to magnetic storms: CHAMP observations, *J. Geophys. Res.*, *110*, A09S29, doi:10.1029/2004JA010908.

Liu, H., H. Lühr, V. Henize, and W. Köhler (2005), Global distribution of the thermospheric total mass density derived from CHAMP, *J. Geophys. Res.*, *110*, A04301, doi:10.1029/2004JA010741.

Liu, H., T. Hirano, and S. Watanabe (2013), Empirical model of the thermospheric mass density based on CHAMP satellite observation, *J. Geophys. Res. Space Physics*, *118*, 843–848, doi:10.1002/jgra.50144.

Liu, X., J. P. Thayer, A. Burns, W. Wang, and E. Sutton (2014a), Altitude variations in the thermosphere mass density response to geomagnetic activity during the recent solar minimum, *J. Geophys. Res. Space Physics*, *119*, 2160–2177, doi:10.1002/2013JA019453.

Liu, X., W. Wang, J. P. Thayer, A. Burns, E. Sutton, S. C. Solomon, L. Qian, and G. Lucas (2014b), The winter helium bulge revisited, Geophys. Res. Lett., 41, 66036609, doi:10.1002/2014GL061471.

Lühr, H., M. Rother, W. Köhler, P. Ritter, and L. Grunwaldt (2004), Thermospheric upwelling in the cusp region: Evidence from CHAMP observations, *Geophys. Res. Lett.*, *31*, L06805, doi:10.1029/2003GL019314.

Lockwood, M., R. Stamper, and M. N. Wild (1999), A doubling of the Suns coronal magnetic field during the past 100 years, *Nature*, *399*, 437–439, doi:10.1038/20867.

Picone, J. M., A. E. Hedin, D. P. Drob, and A. C. Aikin (2002), NRLMSISE-00 empirical model of the atmosphere: Statistical comparisons and scientific issues, *J. Geophys. Res.*, *107*(A12), 1468, doi:10.1029/2002JA009430.

Reigber, C., H. Lühr, and P. Schwintzer (2002), CHAMP mission status, *Adv. Space Res.*, *30*, 129–134.

Rentz, S., and H. Lühr (2008), Climatology of the cusp-related thermospheric mass density anomaly, as derived from CHAMP observations, *Ann. Geophys.*, *26*, 2807–2823.

Richmond, A. D. (1995), Ionospheric electrodynamics using magnetic apex coordinates, *J. Geomagn. Geoelec.*, *47*, 191–212.

Ritter, P., H. Lühr, and E. Doornbos (2010), Substorm-related thermospheric density and wind disturbances derived from CHAMP observations, *Ann. Geophys.*, *28*, 1207–1220, doi:10.5194/angeo-28-1207-2010.

Shepherd, S. G., R. A. Greenwald, and J. M. Ruohoniemi (2002), Cross polar cap potentials measured with Super Dual Auroral Radar Network during quasi-steady solar wind and interplanetary magnetic field conditions, *J. Geophys. Res.*, *107*(A7), doi:10.1029/2001JA000152.

Shim, J. S., et al. (2012), CEDAR Electrodynamics Thermosphere Ionosphere (ETI) Challenge for systematic assessment of ionosphere/thermosphere models: Electron density, neutral density, N_mF_2 and h_mF_2 using space based observations, *Space Weather*, *10*, S10004, doi:10.1029/2012SW000851.

Solomon, S. C., L. Qian, L. V. Didkovsky, R. A. Viereck, and T. N. Woods (2011), Causes of low thermospheric density during the 2007–2009 solar minimum, *J. Geophys. Res.*, *116*, A00H07, doi:10.1029/2011JA016508.

Sutton, E. K., J. M. Forbes, and R. S. Nerem (2005), Global thermospheric neutral density and wind response to the severe 2003 geomagnetic storms from CHAMP accelerometer data, *J. Geophys. Res.*, *110*, A09S40, doi:10.1029/2004JA010985.

518 Sutton, E. K. (2008), Effects of solar disturbances on the thermosphere densities and winds
519 from CHAMP and GRACE satellite accelerometer data, Ph.D. dissertation, Univ. of
520 Colo., Boulder.

521 Sutton, E. K., J. M. Forbes, and D. J. Knipp (2009), Rapid response of the
522 thermosphere to variations in Joule heating, *J. Geophys. Res.*, *114*, A04319,
523 doi:10.1029/2008JA013667.

524 Tapley, B. D., S. Bettadpur, M. Watkins, and C. Reigber (2004), The gravity recovery
525 and climate experiment: Mission overview and early results, *Geophys. Res. Lett.*, *31*,
526 L09607, doi:10.1029/2004GL019920.

527 Thayer, J. P., X. Liu, J. Lei, M. Pilinski, and A. G. Burns (2012), The impact of helium
528 on thermosphere mass density response to geomagnetic activity during the recent solar
529 minimum, *J. Geophys. Res.*, *117*, A07315, doi:10.1029/2012JA017832.

530 Vickers, H., M. J. Kosch, E. Sutton, Y. Ogawa, and C. La Hoz (2013), Thermospheric
531 atomic oxygen density estimates using the EISCAT Svalbard Radar, *J. Geophys. Res.*
532 *Space Physics*, *118*, 1319–1330, doi:10.1002/jgra.50169.

533 Viereck, R., L. Puga, D. McMullin, D. Judge, M. Weber, and W. K. Tobiska (2001),
534 The Mg II index: A proxy for solar EUV, *Geophys. Res. Lett.*, *28*, 1343–1346,
535 doi:10.1029/2000GL012551.

536 Vennerstrøm, S., Moretto, T., Olsen, N., Friis-Christensen, E., Stampe, A. M., and Wa-
537 termann, J. F.: Field-aligned currents in the dayside cusp and polar cap region during
538 northward IMF, *J. Geophys. Res.*, *107*(A8), 1188, doi:10.1029/2001JA009162, 2002.

539 Weimer, D. R. (1995), Models of high-latitude electric potentials derived with a least
540 error fit of spherical harmonic coefficients, *J. Geophys. Res.*, *100*(A10), 19595–19607,

541 doi:10.1029/95JA01755.

542 Weimer, D. R. (1996), A flexible, IMF dependent model of high-latitude electric potentials
543 having "space weather" applications, *Geophys. Res. Lett.*, *23*, 2549–2552.

544 Weimer, D. R. (2005), Improved ionospheric electrodynamic models and application to cal-
545 culating Joule heating rates, *J. Geophys. Res.*, *110*, A05306, doi:10.1029/2004JA010884.

546 Yamazaki, Y., M. J. Kosch, and E. K. Sutton (2015), North-south asymmetry of the
547 high-latitude thermospheric density: IMF BY effect, *Geophys. Res. Lett.*, *42*, 225–232,
548 doi:10.1002/2014GL062748.

549 Zhang, B., W. Lotko, O. Brambles, M. Wiltberger, W. Wang, P. Schmitt, and J. Lyon
550 (2012), Enhancement of thermospheric mass density by soft electron precipitation, *Geo-*
551 *phys. Res. Lett.*, *39*, L20102, doi:10.1029/2012GL053519.

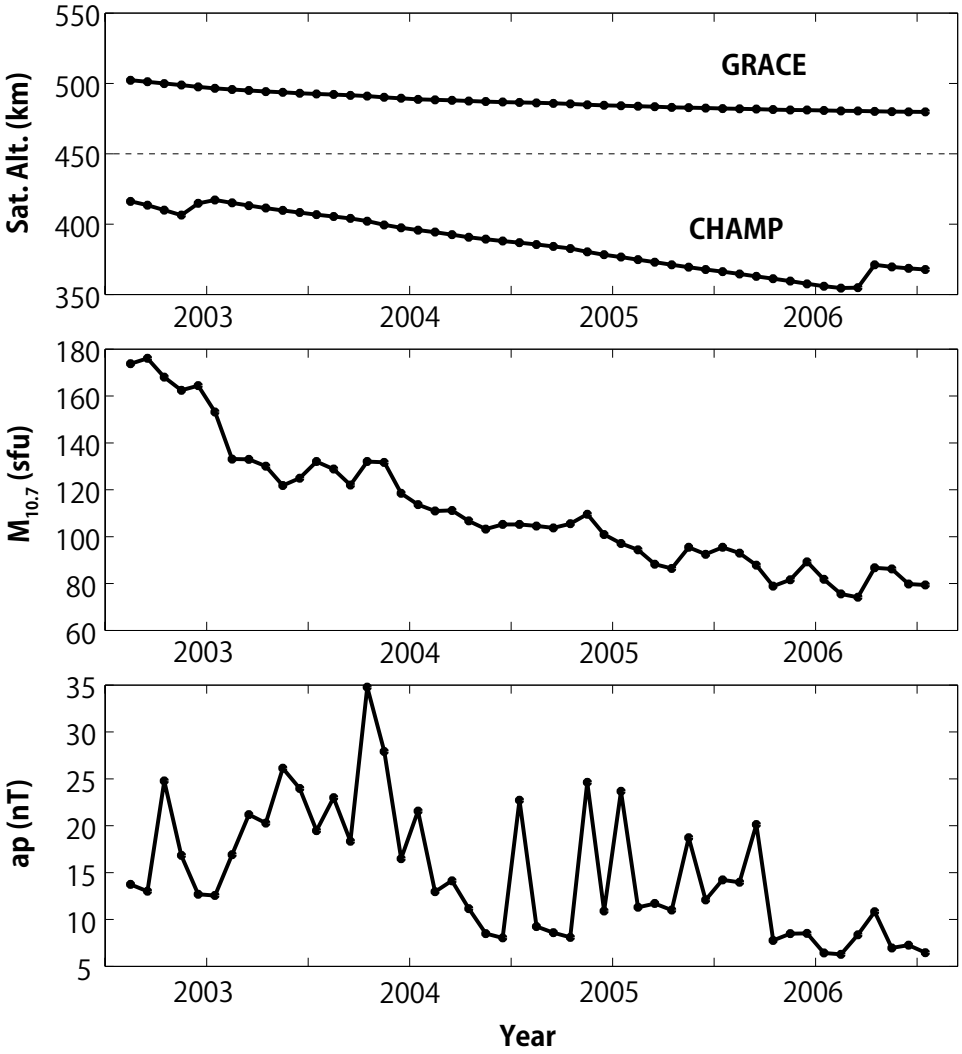

Figure 1. Monthly mean values for (top) CHAMP and GRACE altitudes, (middle) solar activity index $M_{10.7}$ in solar flux unit, and (bottom) geomagnetic activity index *ap* in nano teslas.

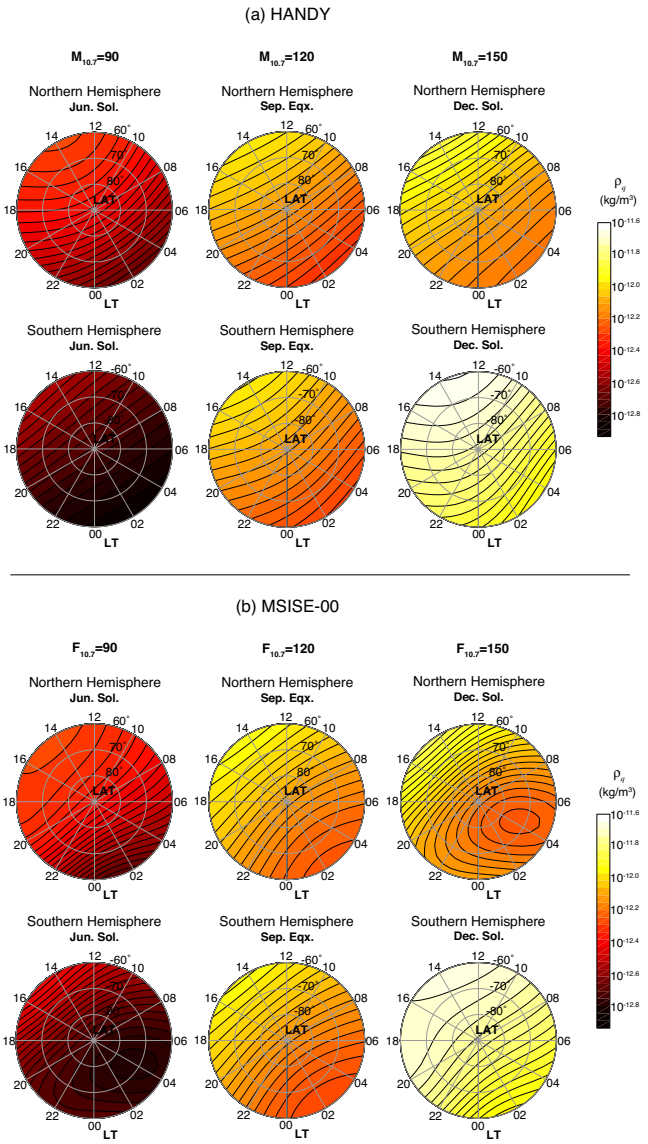

Figure 2. Total mass density of the air at 450 km derived from (a) the HANDY quiet model and (b) the MSISE-00 model. Each panel shows the density distribution as a function of solar local time and geographic latitude. In both (a) and (b), the upper panels are for the Northern Hemisphere and the lower panels are for the Southern Hemisphere. The left panels are for the June solstice condition with a relatively low solar activity input with solar flux indices ($M_{10.7}$ for HANDY and $F_{10.7}$ for MSISE-00) being 90 sfu. The middle panels are for the September equinox condition with the solar flux indices equal to 120 sfu, and the right panels are for the December solstice with relatively high solar activity (the solar flux indices equal to 150 sfu).

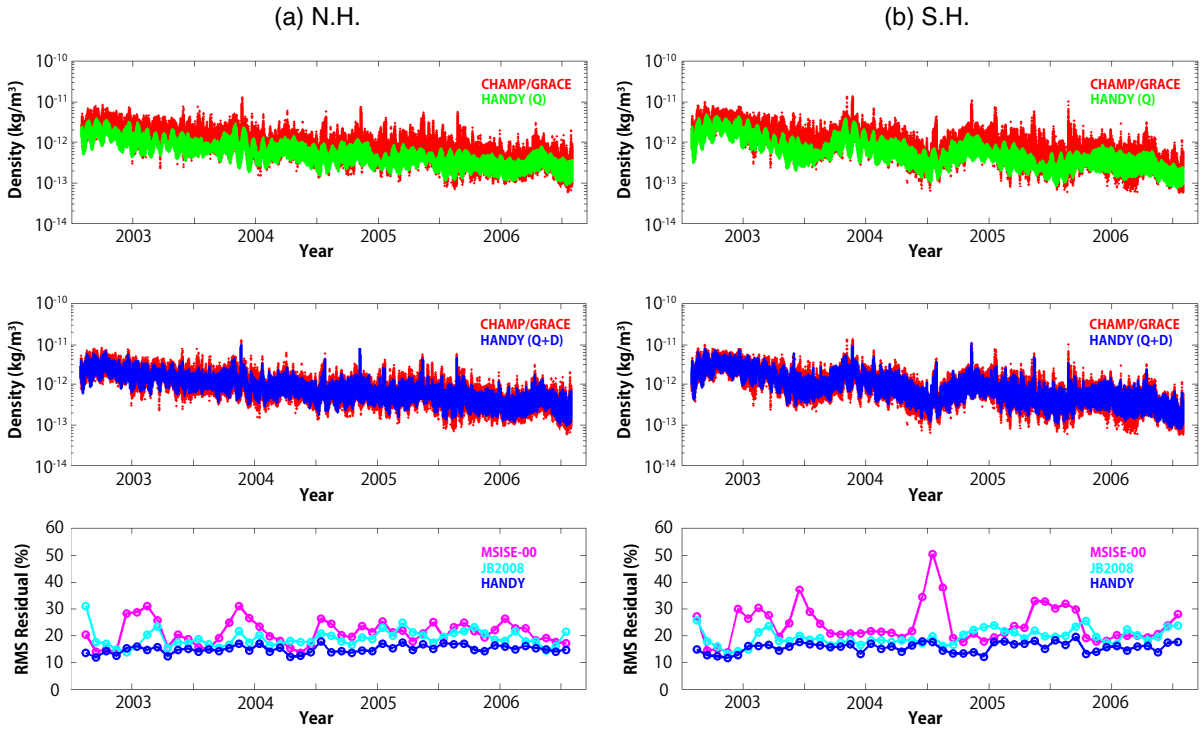

Figure 3. Comparisons between HANDY and CHAMP/GRACE data for (a) the Northern Hemisphere and (b) the Southern Hemisphere. In the top panels, the red dots indicate CHAMP/GRACE measurements and the green dots indicate the corresponding values from the HANDY quiet model. In the middle panels, the red dots are from the measurements and the blue dots are from the HANDY model (the quiet plus disturbance model). The bottom panels show monthly mean values of the root mean square error for (blue) HANDY, (magenta) MSISE-00, and (cyan) JB2008

.

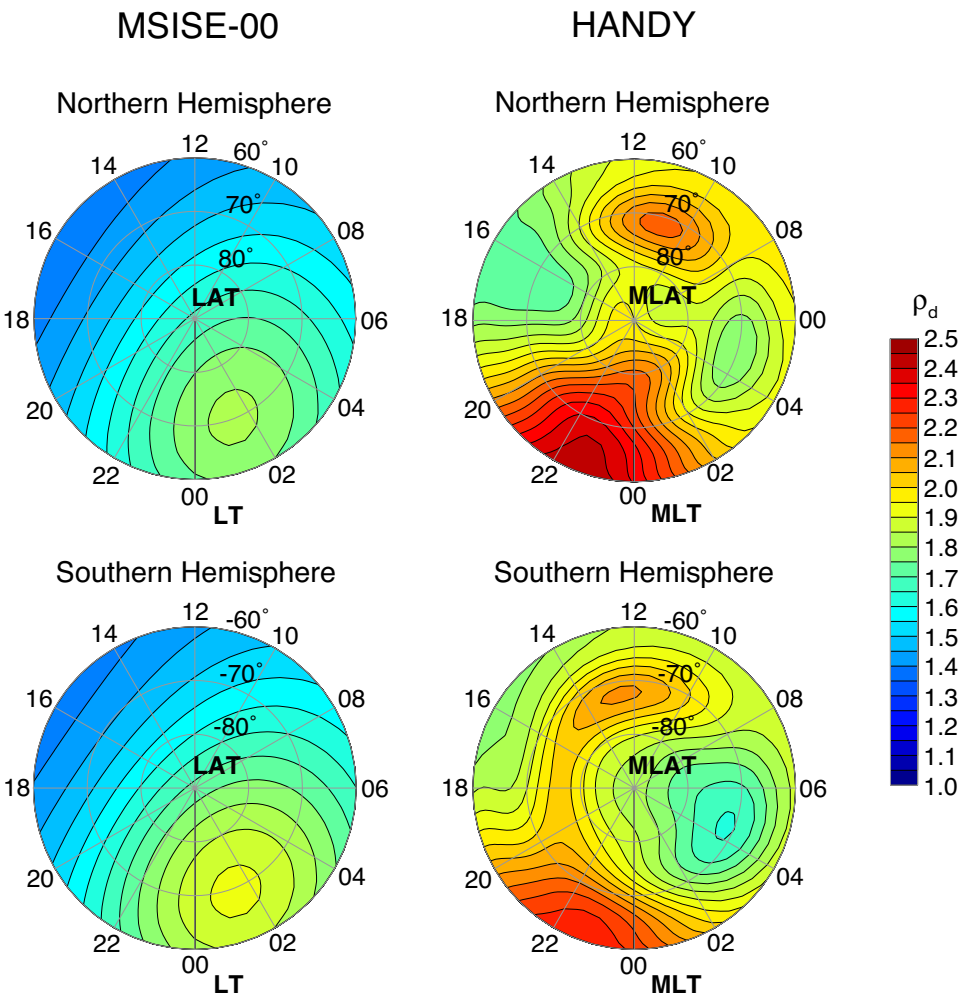

Figure 4. The relative density perturbation at 450 km from (left) the MSISE-00 model and (right) the HANDY model for the September equinox condition in (top) the Northern Hemisphere and (bottom) the Southern Hemisphere. The density perturbations are given as the ratio between the quiet-time and non quiet-time calculations. For MSISE-00, the quiet-time densities are computed for ap=0 nT, and the non quiet-time densities are obtained for ap=27 nT. For HANDY, the non quiet-time densities are calculated with E_{SW}=3.3 mV/m, P_{SW}=3.1 hPa, and C_{SW}=180°, which approximately corresponds to ap=27 nT.

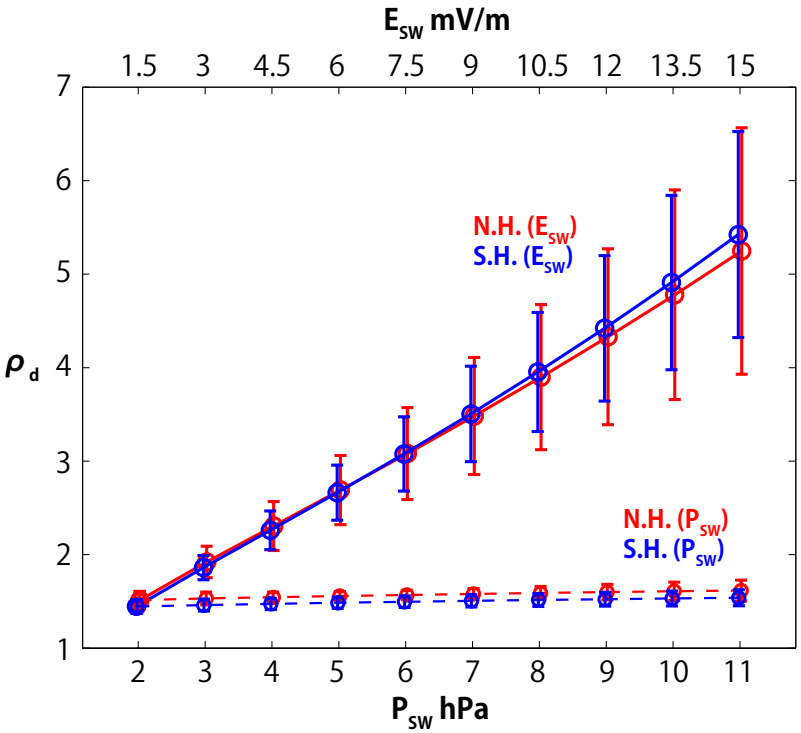

Figure 5. The relative density perturbation due to changes in the solar wind electric field magnitude E_{SW} and solar wind dynamic pressure P_{SW}, derived from HANDY. The solid lines show the results for the E_{SW} response and the dashed lines show the results for the P_{SW} response. E_{SW} values are given on the top of the panel while P_{SW} values are given in the bottom of the panel. The other model inputs are: $M_{10.7}$=120 sfu, DoY=264, and C_{SW}=180°. The red lines show the average for the Northern Hemisphere (poleward of 60° magnetic latitude), and the blue lines show the average for the Southern Hemisphere (poleward of -60° magnetic latitude).

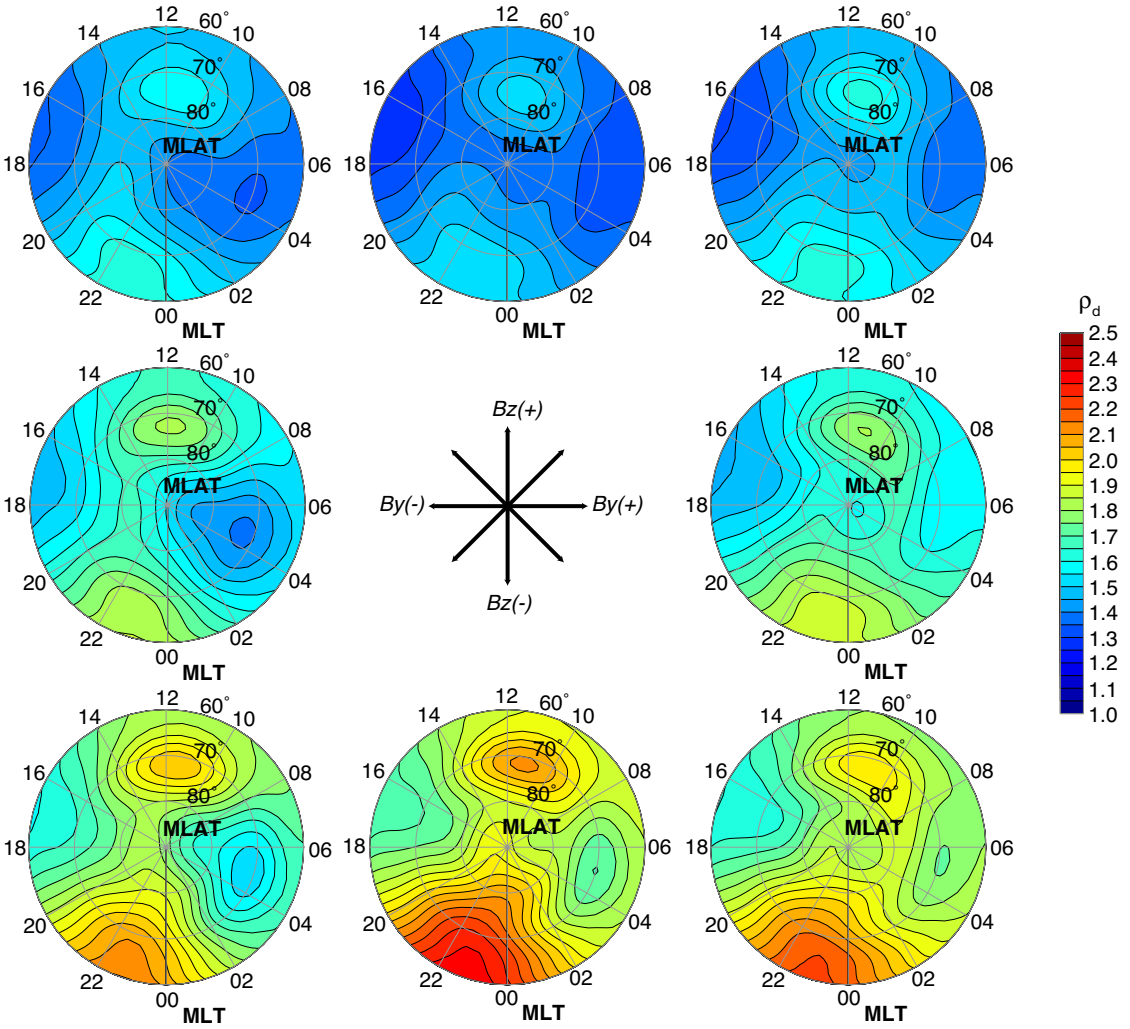

Figure 6. The relative density perturbation at 450 km derived from the HANDY model for the Northern Hemisphere. The IMF clock angles are 0°, 45°, 90°, 135°, 180°, 225°, 270°, and 315°, clockwise from the top middle panel. Other model inputs are: $M_{10.7}$=110 sfu, DoY=264, E_{SW}=2.8 mV/m and P_{SW}=2.7 hPa, which approximately correspond to ap=18 nT.

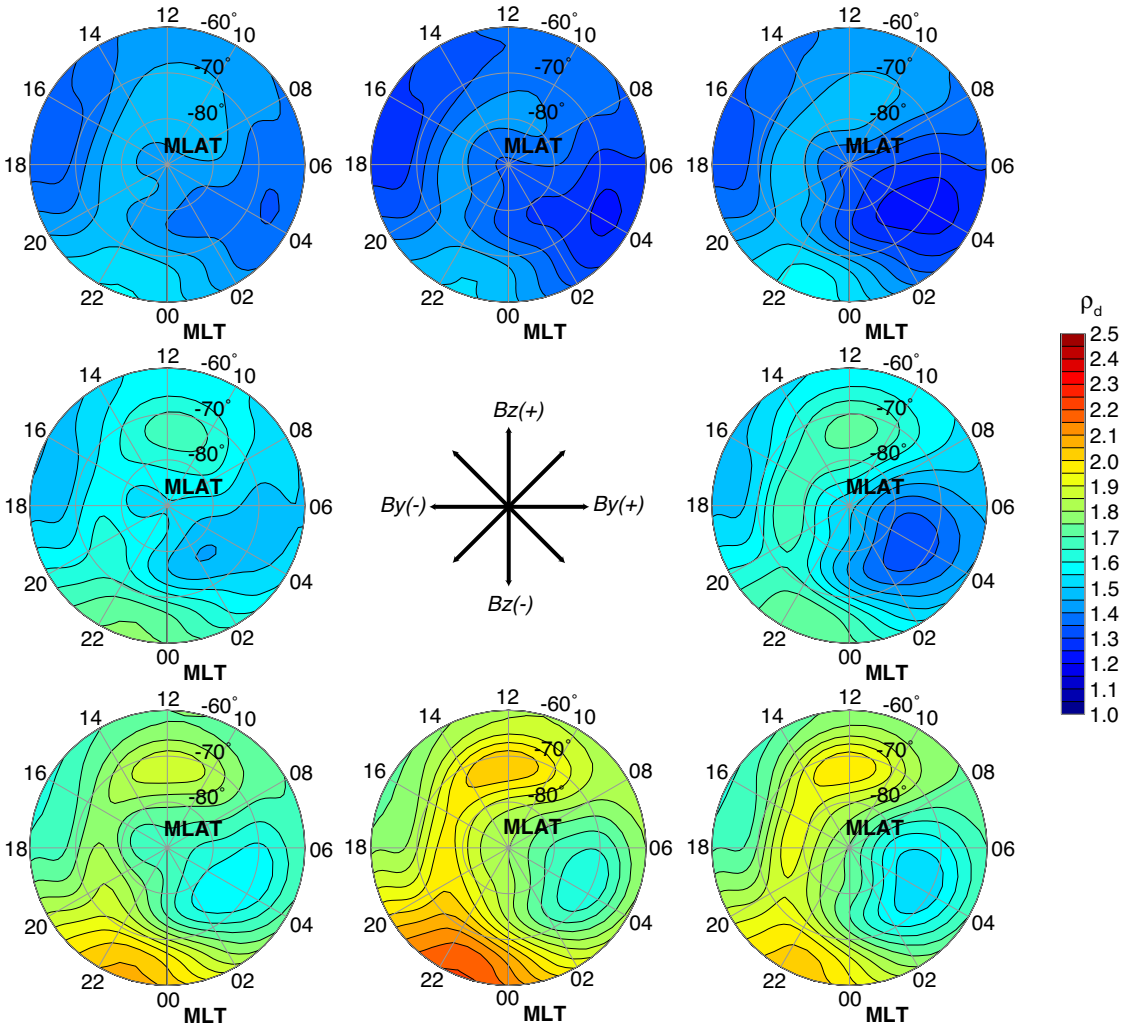

Figure 7. The same as Figure 6 but for the Southern Hemisphere.

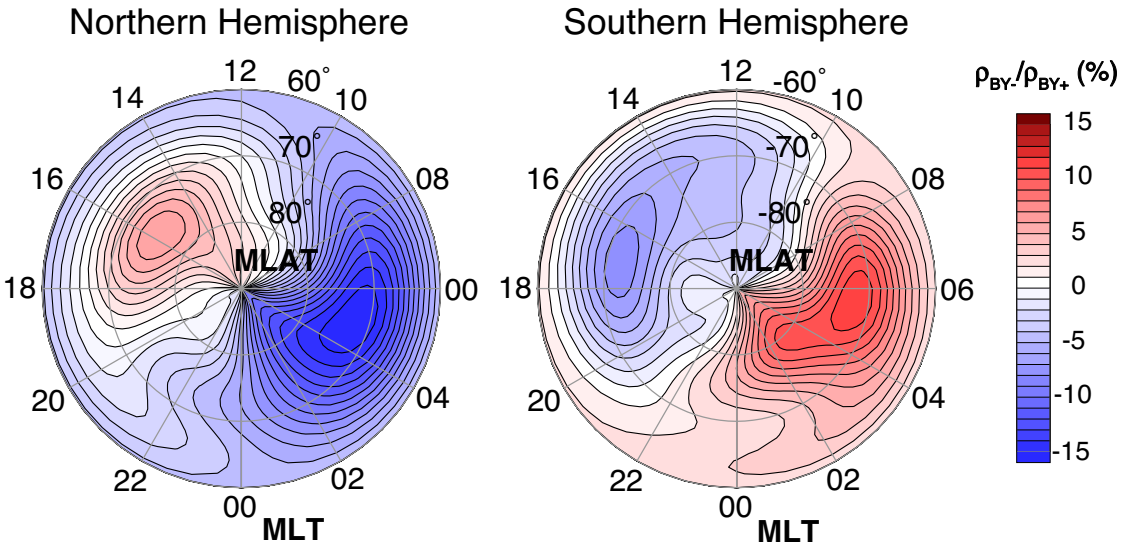

Figure 8. The effect of the IMF B_y on the high-latitude thermospheric density at 450 km for (left) the Northern Hemisphere and (right) the Southern Hemisphere. The density ratios are derived from HANDY for C_{SW}=90° and for C_{SW}=270°. Other model inputs are: $M_{10.7}$=150 sfu, DoY=172, E_{SW}=3.3 mV/m and P_{SW}=3.1 hPa, which approximately correspond to ap=27 nT.

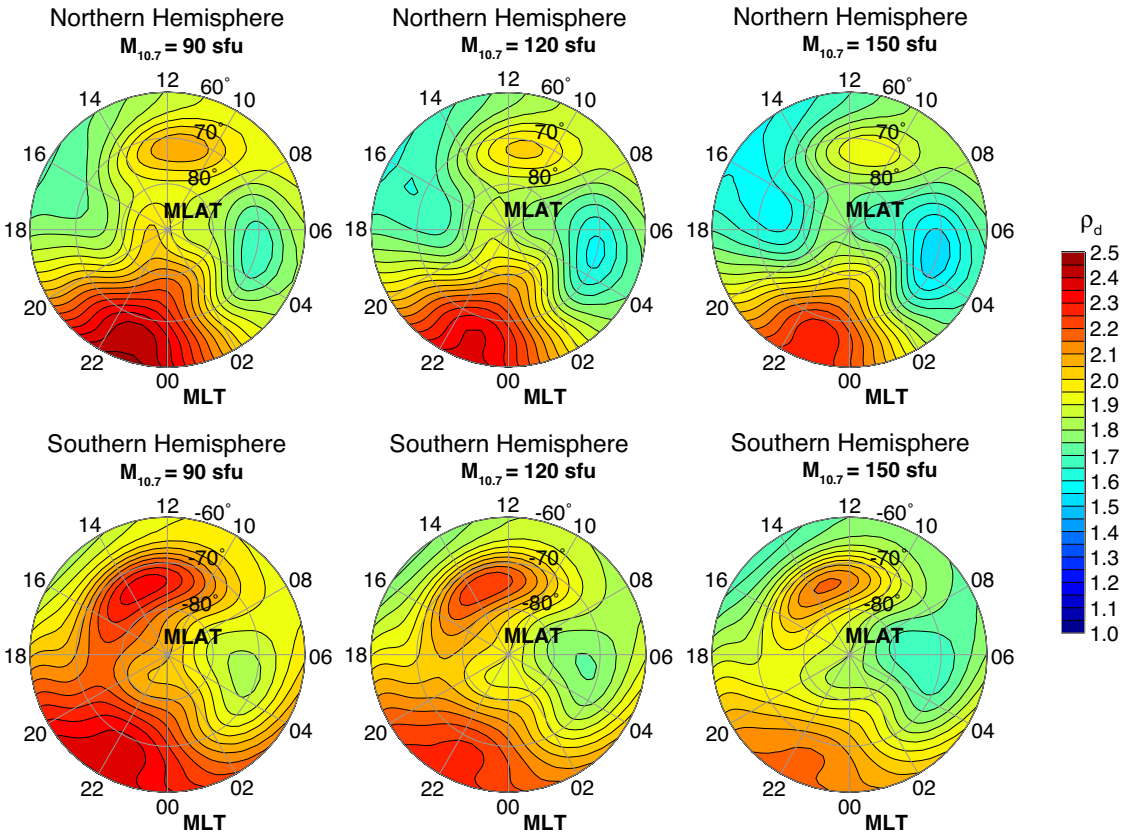

Figure 9. The relative density perturbation at 450 km at different solar activity conditions. The densities are derived from HANDY with $M_{10.7}$=90 sfu, $M_{10.7}$=120 sfu, and $M_{10.7}$=150 sfu for (top) the Northern Hemisphere and (bottom) the Southern Hemisphere. Other model inputs are DoY=80, E_{SW}=2.8 mV/m, C_{SW}=180° and P_{SW}=2.7 hPa.

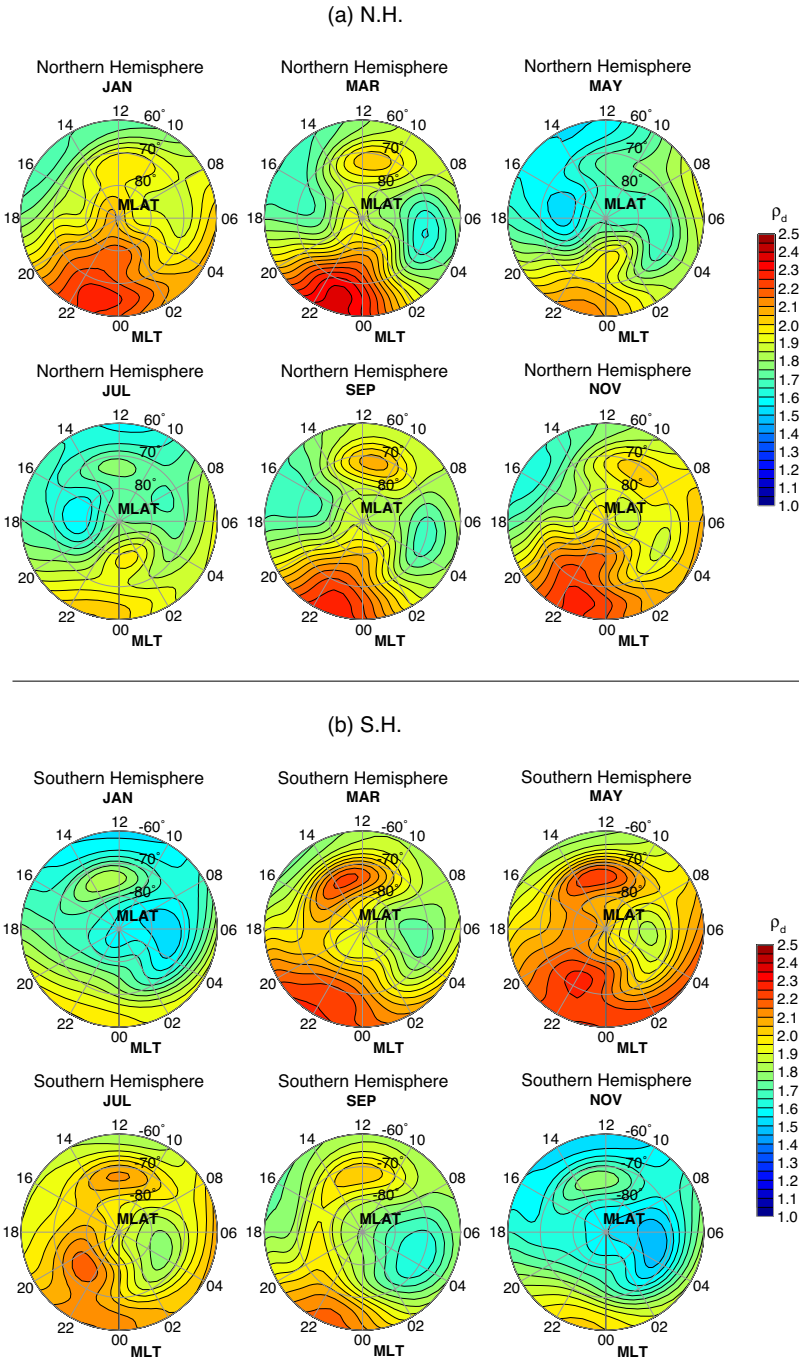

Figure 10. The relative density perturbation at 450 km derived from HANDY for (a) the Northern Hemisphere and (b) the Southern Hemisphere for different months: January (DoY=15), March (DoY=74), May (DoY=135), July (DoY=196), September (DoY=258), and November (DoY=319). Other model inputs are: $M_{10.7}$=120 sfu, E_{SW}=2.8 mV/m, C_{SW}=180° and P_{SW}=2.7 hPa.